metals

MDPI

Article

Temperature Based Fatigue Damage Entropy for Assessment of High-Cycle Fatigue in Laser-Welded Joints

Yang Liu, Yang Sun and Xinhua Yang *

School of Materials Science and Engineering, Dalian Jiaotong University, Dalian 116028, China; ly_19970208@163.com (Y.L.)
* Correspondence: yangxh@djtu.edu.cn

Abstract

To quickly predict the fatigue strength of welded joints in high-cycle fatigue tests and fit the S-N curve, this paper proposes a new model based on infrared thermal imaging technology. High-cycle fatigue tests were conducted on laser-welded joints of weathering steel Q450NQR1 and separately, on joints made of stainless steel T4003, while local temperature variations in the joints were monitored. Based on the experimentally observed temperature drop behavior, a novel Temperature-Drop-Curve-Based Fatigue Damage Entropy (TDC-FDE) model was developed to rapidly estimate the fatigue life and fatigue limit of welded joints. The model quantifies the entropy generated during fatigue damage evolution based on the temperature-decrease slope and establishes a direct relationship between entropy and the fatigue performance of the joint using this slope as the linking parameter. Experimental results indicate that a material's specific heat capacity, density, elastic modulus, and applied stress level directly influence fatigue damage entropy generation. The entropy increase associated with purely elastic deformation does not contribute to fatigue damage in high-cycle fatigue; therefore, this portion should be excluded from the fatigue damage entropy calculation. The fatigue damage entropy of a given weld joint tends to remain nearly constant under different stress levels and loading frequencies. Finally, traditional fatigue tests demonstrated that the maximum deviation between the fatigue strength predicted by the proposed model and the experimentally measured values does not exceed 3.4%, thereby verifying the model's accuracy and effectiveness in evaluating fatigue performance.

Keywords: fatigue damage assessment; laser welding; temperature drop curve; high-cycle fatigue; infrared thermography

Academic Editor: Giovanni Meneghetti

Received: 30 October 2025
Revised: 23 November 2025
Accepted: 26 November 2025
Published: 27 November 2025

Citation: Liu, Y.; Sun, Y.; Yang, X. Temperature Based Fatigue Damage Entropy for Assessment of High-Cycle Fatigue in Laser-Welded Joints. *Metals* **2025**, *15*, 1306. https://doi.org/10.3390/met15121306

Copyright: © 2025 by the authors. Licensee MDPI, Basel, Switzerland. This article is an open access article distributed under the terms and conditions of the Creative Commons Attribution (CC BY) license (https://creativecommons.org/licenses/by/4.0/).

1. Introduction

Fatigue is a significant contributor to the failure and functional degradation of metallic components subjected to fluctuating stresses [1–3]. Welding is a critical connection method commonly applied in shipbuilding, aerospace, rail transportation, and other industries. The precise and timely assessment of fatigue performance in welded structures is of paramount importance to industrial manufacturing. Based on the analysis of fatigue failure in welded structures under various load forms using thermodynamic parameters, quantifying fatigue damage has proven feasible. Consequently, mathematical models based on thermodynamic parameters are increasingly applied in this field [4–6].

This project establishes a fatigue performance evaluation model for the welded structures and validates it against experimental data to enhance the accuracy of fatigue performance predictions based on thermal imaging technology. Researchers proposed the Luong [7,8] and Risitano [9,10] methods to determine a material's fatigue strength. These methods involve identifying the fatigue limit either by locating the intersection points of temperature rise fitting lines at various stress levels or by finding the intersection between the temperature rise fitting line (above the fatigue strength) and the horizontal axis. These approaches utilize the relationship between temperature evolution and applied stress levels to estimate fatigue limits. Temperature changes are inherently associated with energy dissipation and an increase in entropy within the local region of the specimen. Consequently, to more effectively quantify fatigue strength and fatigue life, it is essential to precisely calculate both energy dissipation and entropy variations throughout the fatigue process. Fluctuations in local specimen temperature during fatigue testing are inevitably accompanied by energy dissipation and corresponding changes in thermodynamic entropy. Given the established relationship between local energy dissipation, entropy increase, and material fatigue damage, fatigue damage is examined and quantified using thermodynamic parameters. Khonsari et al. [11,12] monitored the surface temperature of specimens subjected to fatigue under various loading conditions: tensile, torsion, and bending. The test results indicated that the temperature rise slope R_θ determines energy changes, which lead to the derivation of a specific indicator for characterizing fatigue performance-fatigue fracture entropy (FFE). Jirandehi et al. [13] and Liakat et al. [14] demonstrated that fatigue fracture entropy is a material-specific property and does not depend on factors such as geometry, loading frequency, and form of loading.

The energy dissipation resulting from changes in the local temperature of the specimens plays a pivotal role in the calculation of fatigue damage entropy. Consequently, a comprehensive analysis of all energy dissipation throughout the fatigue process is fundamental for determining fatigue damage entropy. Here, Q_t represents the total energy dissipation of the local specimen, Q_f is the energy dissipation caused by the "internal friction" of atoms oscillating about their equilibrium positions, and Q_i denotes the irreversible energy dissipation. Based on the principle that fatigue damage entropy remains constant, a quantitative assessment of material fatigue damage is feasible. Numerous scholars have investigated this concept extensively. To investigate the influence of energy dissipation components Q_f and Q_i within the total energy dissipation Q_t on evaluating fatigue strength at stress levels below the fatigue limit, Mehdizadeh et al. [15] conducted strain-controlled low-cycle bending fatigue tests on homogeneous materials, specifically stainless steel 304 and carbon steel 1018. The research indicated that Q_i serves as a key factor in calculating fatigue damage entropy, while the contribution of Q_f to fatigue damage is negligible. Consequently, to ensure more accurate predictions in calculating fatigue damage entropy, Q_f should be subtracted from the total energy dissipation Q_t. Amooie and Khonsari [16] demonstrated that fatigue life increases as ambient temperature decreases. Within the temperature range of −10 °C to 20 °C, the energy dissipated per cycle in low-temperature environments remains relatively low, though the cumulative dissipated energy over time is substantial. Moreover, the fatigue damage entropy is observed to be constant across different ambient temperatures. Mahmoudi et al. [17] conducted low-cycle fatigue tests on various alloys, including Al7075-T6 and MCS1045, to validate the accuracy of the entropy-kinetic model predictions based on the temperature rise slope. Researchers observed that, due to the differing physical properties of steel and aluminum alloys, the steady-state temperature of steel is substantially higher than that of aluminum alloys under equivalent stress levels. It should be noted that two widely used methods are currently available for calculating energy dissipation Q in fatigue analysis: a temperature rise slope-based method, applicable to both high- and low-cycle fatigue [18], and a hysteresis loop

area-based method, specifically suitable for low-cycle fatigue [19]. Energy dissipation is an essential link between temperature evolution and fatigue fracture entropy. The accuracy of energy dissipation is essential to the magnitude of fatigue damage entropy, which, in turn, influences the precision of fatigue performance evaluation. Unlike the calculation of energy dissipation in standard welded fatigue specimens during high-cycle fatigue tests, the calculation for welded structures encounters the following two challenges: firstly, during the fatigue test, the stress levels remain below the material's yield strength, making it difficult to monitor the hysteresis loop. Therefore, calculating energy dissipation from the hysteresis loop area is not feasible. Secondly, the temperature rise slope, R_θ, is influenced by uncontrollable factors such as welded joint-induced deformation and defects, which cause significant variations in the slope at the same stress level. This, in turn, affects the calculation of energy dissipation, leading to excessive discreteness in the fatigue fracture entropy and reduced accuracy in fatigue assessment.

Current research on the fatigue performance of welded joints using infrared thermal imaging technology primarily focuses on temperature variations, while studies on the mechanisms of energy dissipation and entropy increase in welded joint fatigue remain relatively limited. Ummenhofer and Medenberg [20] employed infrared thermography to distinguish the linear temperature rise from the nonlinear temperature rise in order to determine the fatigue limit of welded joints. The location of crack initiation and the moment of fracture were determined by analyzing the peak temperature in the thermal phase diagram. Wei et al. [21–23] conducted high-cycle fatigue tests on Q460 butt joints and Q310NQL2-Q345NQR2 laser-welded butt joints, monitoring the temperature evolution of test specimens to develop an effective fatigue fracture entropy evaluation model. Experimental results indicated that both the fatigue fracture entropy and fatigue life of these welded joints followed a normal distribution. Furthermore, the study derived the generation of anelastic entropy at low stress levels and irreversible entropy at high stress levels. The predicted P-S-N curve showed strong consistency with experimental findings, supporting the model's accuracy. Crupi et al. [24] estimated the fatigue strength of AH36 steel butt joints using infrared thermography and compared it with results obtained through conventional testing methods. The experimental results showed that a small error between the two methods, and the S-N curve was accurately fitted using infrared thermography. Yan et al. [25] employed variations in temperature rise across different stress levels to predict the fatigue strength of two types of AZ31B magnesium alloy welded joints in high-frequency fatigue tests. The predicted results deviated by approximately 10% from the experimental data.

It is worth noting that, for the fatigue performance evaluation method of welded joints using infrared thermal imaging, the calculation of fatigue damage entropy is based on the temperature rise phase of the specimen's surface during the fatigue test. Although fatigue damage entropy can be determined from the temperature rise slope of the specimen surface, this method faces inherent challenges, including significant variability in fatigue fracture entropy and substantial deviations between experimental and predicted outcomes. The intrinsic physical properties of specific welded joints—such as specific heat capacity, thermal conductivity, and elastic modulus—remain constant throughout the test [26–28]. As a result, once the fatigue test concludes, the temperature decay curves for the same material across varying stress levels exhibit a consistent pattern, which significantly reduces the variability in the initial temperature rise slope caused by factors such as welding defects and stress concentration. Utilizing the consistent temperature decay curve of a specific welded structure, this study employs the slope of temperature decay at steady-state temperatures across various stress levels to calculate the energy dissipation. This project establishes a fatigue performance evaluation model for the welded structures and

validates it against experimental data to enhance the accuracy of fatigue performance predictions based on thermal imaging technology.

In summary, because the hysteresis loop is difficult to measure during high-cycle fatigue testing of welded joints, the assessment of energy dissipation in such tests relies primarily on infrared thermography. Currently, the characterization of high-cycle fatigue performance of welded joints using infrared thermography predominantly relies on the initial temperature rise slope. However, the temperature rise slope can be influenced by welding defects and deformations, leading to considerable variability and necessitating extensive computational effort. Therefore, this study employs the temperature drop curve measured after specimen fatigue failure as the basis for calculating energy dissipation and fatigue damage entropy (FDE). High-cycle fatigue tests were conducted on the laser-welded joints of weathering steel Q450NQR1 and stainless steel T4003. This study monitored the temperature evolution at the stress concentration point (weld toe area) of the joints during the fatigue test to capture the temperature change in the weld toe area under varying stress levels. The energy dissipation and fatigue damage entropy are calculated using the temperature drop slope at the steady-state temperature following the failure of the fatigue specimens. The fatigue life at a specific stress level is determined using the fatigue damage entropy. The S-N curve for the welded joints is generated, and a fatigue fracture entropy-based performance evaluation model is developed. The accuracy of the proposed model is validated through experimental testing.

2. Theory

2.1. Temperature Evolution and Energy Dissipation

Microplastic deformation and the nucleation of fatigue microcracks in the local material of the welded joint are the primary mechanisms that ultimately lead to fatigue fracture. The ease or difficulty of crack nucleation is influenced by factors such as grain size [29–31], dislocation density [32], surface morphology, and welding defects. During the fatigue test, the microplastic deformation and elastic behavior within materials are reflected in changes in the surface temperature of the fatigue specimen, as well as energy dissipation. Figure 1a illustrates that the local temperature evolution of the specimen surface can be categorized into four stages [33]: the initial phase is characterized by a rapid increase in the specimen's surface temperature at the commencement of the fatigue tests. Subsequently, the temperature attains a stable state and reaches the steady-state temperature, denoted as T_s. The third stage is characterized by a rapid increase in the temperature of the localized area of the fatigue specimen, attaining the maximum temperature observed throughout the temperature evolution process at the moment of fracture. Finally, the fourth stage encompasses the period during which the local peak temperature of the specimen decreases to ambient temperature after fatigue failure. The steady-state temperature during the second stage is directly proportional to the local stress level of the specimen, while the thermoelastic effect is influenced by both the loading frequency and the ambient temperature [34]. At present, research on energy dissipation in fatigue tests is primarily based on the temperature rise slope of the initial temperature. However, the initial temperature rise slope demonstrates considerable variation due to factors such as welding deformation, residual stress, and surface morphology, even when fatigue parameters-such as stress level, loading frequency, and stress ratio-are identical. This variation presents a challenge for analyzing fatigue failure in welded structures using infrared thermal thermography. As illustrated in Figure 1b, the curves representing the decrease in the specimen's peak temperature to ambient temperature following fatigue failure are consistent. The slope of the temperature decline phase during cooling after the specimen's fracture can be utilized to more precisely calculate the energy dissipation Q_i responsible for fatigue failure, thus enhancing the accuracy of the fatigue life prediction model [35].

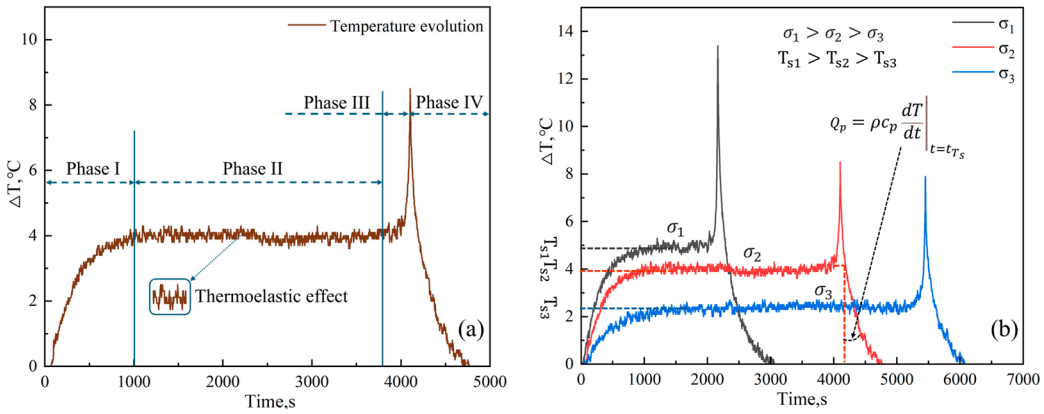


Figure 1. Schematic diagram of temperature evolution of welded joints and the calculation of the temperature drop slope at steady-state temperature. (**a**) Schematic diagram of temperature evolution. (**b**) Schematic diagram of energy dissipation calculation using the temperature drop slope.

As discussed in Section 1, the total energy dissipation Q_t comprises the energy dissipation Q_f due to the oscillation of atoms at their equilibrium positions, and the energy dissipation Q_i resulting from microplastic deformation of the local material. The second component of energy dissipation Q_i, arises from the microplastic deformation of local materials. According to the fatigue damage accumulation theory, this portion of energy dissipation can precisely quantify the extent of fatigue damage in materials during fatigue testing [36–38]. Figure 2 illustrates the distribution of energy dissipation in the material during fatigue failure. Numerous studies on homogeneous materials have shown that in high-cycle tests, when the stress level is below the fatigue limit, the energy dissipation Q_f results from recoverable elastic deformation, and this component of energy dissipation does not contribute to fatigue damage [39,40]. However, when the stress level exceeds the fatigue limit, most of the energy dissipation Q_i is attributable to irreversible material damage, making Q_i a critical factor in assessing the material's fatigue damage.

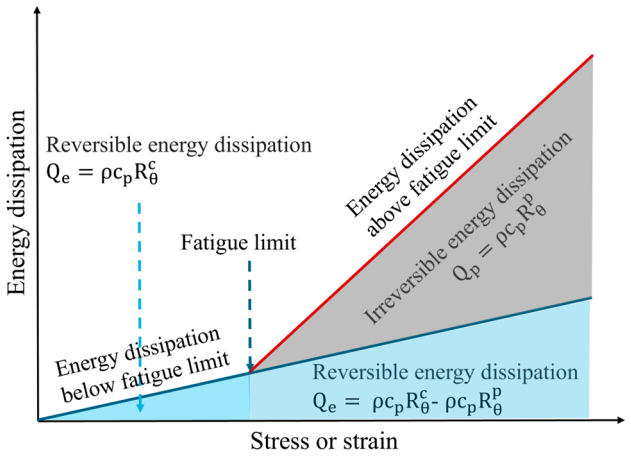


Figure 2. Schematic diagram of the relationship between stress/strain and energy dissipation.

2.2. Fatigue Damage Entropy Model for Welded Joints

To address inaccuracies in structural prediction caused by welded joint-induced deformation and defects impacting the temperature rise slope in the fatigue damage entropy model, this paper develops a mathematical model for calculating the fatigue damage entropy of welded joints using the temperature drop method, aimed at enhancing the prediction accuracy of existing models. To describe the energy transformation process within the local area of the welded joint during the fatigue test, we present the following formula derived from the classic first law of thermodynamics:

$$dU = \dot{E}_{in} + \dot{E}_{gen} - \dot{E}_{out} \tag{1}$$

$\dot{E}_{gen}$ denotes the energy dissipation resulting from both elastic behavior and microplastic deformation within the joint's local area. Therefore, $\dot{E}_{gen} = Q_t$, where Q_t represents the total energy dissipation resulting from both elastic and inelastic behavior within the joint's local area. Among them, $\dot{E}_{in}$ and $\dot{E}_{out}$ represent the energy exchange between the local area of the welding joint and the surrounding environment, and U represents the change in stored energy in the local area. Given that the temperature of the joint's local area is consistently higher than the ambient temperature during the fatigue test, $\dot{E}_{in}$ can be neglected. $\dot{E}_{out}$ denotes the energy emitted by the welded joint to the environment via heat conduction, radiation, and convection. Existing research [41,42] indicates that, when calculating energy dissipation from temperature changes, the energy exchange through these mechanisms can be disregarded. Therefore, the energy equation for the local area of the welded joint can be expressed as follows:

$$\dot{E}_{gen} = U = Q_t = Q_f + Q_i \tag{2}$$

Energy dissipation in high-cycle fatigue can be categorized into two components based on the stress level relative to the fatigue limit: When the applied stress level is below the fatigue limit, energy dissipation results from recoverable elastic behavior, with irrecoverable microplastic deformation not contributing to energy dissipation. Conversely, when the stress level exceeds the fatigue limit, the local energy dissipation in the joint includes both elastic and microplastic behavior.

$\sigma < \sigma_{FL}$:

$$Q_t = Q_f = \rho c_p R_\theta^c = \rho c_p \frac{dT}{dt}\Big|_{t=T_s} \tag{3}$$

$$Q_i = 0 \tag{4}$$

$\sigma > \sigma_{FL}$:

$$Q_t = Q_f + Q_i = \rho c_p R_\theta^c = \rho c_p \frac{dT}{dt}\Big|_{t=T_s} \tag{5}$$

$$Q_p = Q_t - Q_f = \rho c_p (R_\theta^c - R_\theta^e) \tag{6}$$

where ρ is the material density, c_p is the specific heat capacity, R_θ^c is the temperature drop slope corresponding to the steady-state temperature T_s, and R_θ^e represents the temperature drop slope that does not contribute to fatigue damage. According to the second law of thermodynamics, the fatigue damage entropy (thermodynamic entropy) of the local joint remains greater than zero throughout the fatigue test loading process. This premise serves as the foundation for developing a fatigue damage prediction model. According to this model, the increase in local entropy of the joint is defined as follows:

$$\dot{S}_i = \frac{\sigma : \dot{\varepsilon}}{T} - \frac{\vec{q} . \overrightarrow{grad T}}{T^2} - \frac{A_i \dot{V}_i}{T} \geq 0 \tag{7}$$

σ and $\dot{\varepsilon}$ represent the stress tensor and the corresponding strain tensor, respectively; T denotes the absolute temperature; $\vec{q}$ signifies the heat flux; $A_i \dot{V}_i$ denotes the relevant quantity related to the internal state of the material; and $\dot{V}_i$ represents the conjugate thermodynamic force related to A_i. Multiplying both sides of Equation (7) by the absolute temperature T yields Equation (8):

$$T\dot{S}_i = \sigma : \dot{\varepsilon} - \frac{\vec{q} \cdot \overrightarrow{grad T}}{T} - A_i \dot{V}_i \geq 0 \tag{8}$$

where $W = \sigma : \varepsilon,\ Q = T\dot{S}_i$. Therefore, Equation (8) elucidates the relationship between local energy dissipation and the welded joint. The three terms in the middle of Equation (8) denote distinct factors that contribute to energy dissipation. $\sigma : \dot{\varepsilon}$ denotes the power performed by stress and strain. $\frac{\vec{q} \cdot \overrightarrow{\mathrm{grad}} T}{T}$ denotes the heat flux resulting from heat conduction. In high-cycle fatigue tests, this term can be neglected, as the temperature gradient is minimal during the second stage of temperature evolution. $A_i V_i$ is a parameter associated with the internal state of the material. The energy dissipation attributed to $A_i V_i$ resulting from the work performed by stress and strain constitutes only 5% to 10% of the total energy dissipation [43,44]. Consequently, this term may be omitted when evaluating energy dissipation in high-cycle fatigue. Since the final two terms on the right-hand side of Equation (8) are disregarded, Equation (8) is reduced to $W = Q$. W is defined as $W = \sigma : \varepsilon$, and $\varepsilon = \frac{\sigma}{E}$. Additionally, $Q_p = \rho c_p R_\theta^c$ denotes the dissipation of energy per stress cycle. The entropy production during each stress cycle can, therefore, be described using the following two equations:

$$\dot{S}_i = \frac{\rho c_p R_\theta^c}{f \Delta T_s} \tag{9}$$

$$\dot{S}_i = \frac{\sigma^2}{E T_s} \tag{10}$$

where ΔT_s represents the steady-state temperature, and ΔT_s is equal to the difference between the local temperature of the specimen and the initial temperature. The accumulation of fatigue damage entropy extends from the initiation of the fatigue test ($t = 0$) to the point of fatigue fracture ($t = t_f$). The fatigue damage entropy, which remains constant, functions as an indicator of the component's fatigue life. Therefore, the total entropy during this period is determined by integrating Equation (11):

$$S = \int_{t_f}^{0} \frac{Q_i}{T} dt \tag{11}$$

The temperature evolution curve during the fatigue test indicates that the temperature remains at the steady state value T_s for the majority of the fatigue process, during which most fatigue damage takes place. As a result, setting $T = \Delta T_s$ in the above equation and substituting Equation (12) gives

$$S = \int_{t_f}^{0} \frac{\rho c_p R_\theta^p}{\Delta T_s} dt \tag{12}$$

The fatigue test time is given by $t_f = N_f$ denotes the number of cycles to failure, and f represents the loading frequency. By substituting $t_f = \frac{N_f}{f}$ into Equation (13), the fatigue damage entropy of the local joint during the fatigue test can be calculated.

$$FDE = \frac{\rho c_p (R_\theta^c - R_\theta^e) N_f}{\Delta T_s f} = \frac{\rho c_p R_\theta^p N_f}{\Delta T_s f} \tag{13}$$

3. Experimental Procedures

In this study, 5 mm thick weathering steel Q450NQR1 and ferritic stainless steel T4003 were used as base materials, respectively, and two types of laser-welded joints fabricated from them were selected as the research subjects. Fatigue performance was analyzed using the fatigue damage entropy model, and the accuracy of the model's result was validated through comparison with experimental results. The mechanical properties of weathering steel Q450NQR1 and stainless steel T4003 are provided in Table 1, while their chemical compositions are detailed in Table 2 and Table 3, respectively. Both types of

joints were fabricated using a nitrogen-shielded laser welding process, and the corresponding welding process parameters are listed in Table 4. As illustrated in Figure 3, prior to the fatigue test, a matte black paint layer was applied to the specimen's surface to improve emissivity and reduce infrared reflection. The local temperature variations on the specimen's surface were continuously monitored using an infrared thermograph positioned 50 cm away and perpendicular to the specimen's surface. To enhance the precision of monitoring local temperature variations in the joint, a Fluke-Ti450 infrared thermal imager (Fluke Corporation, Everett, WA, USA) was utilized to measure and record the surface temperature of the specimen. The infrared thermal imager used in this study features an image capture frequency of 9 Hz, a resolution of 320 × 240 pixels, and a thermal sensitivity of ≤0.03 °C at a target temperature of 30 °C (30 mK).

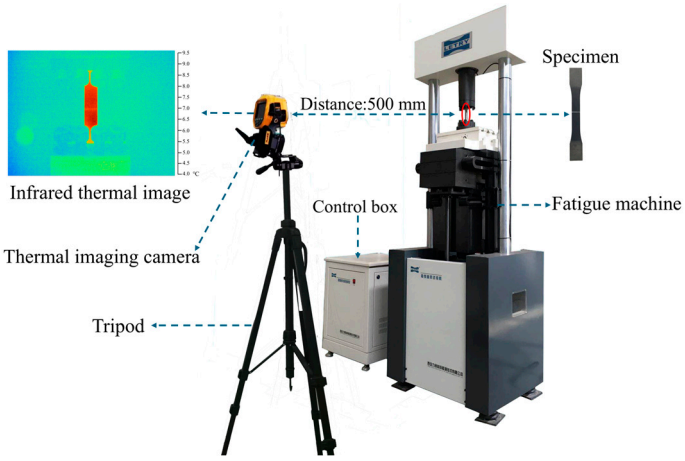


Figure 3. Schematic diagram of the experiment equipment.

Table 1. Mechanical and physical properties of materials.

Material	Yield Tensile Strength	Ultimate Tensile Strength	Density	Specific Heat Capacity	Thermal Conductivity
Q450NQR1	450 MPa	550 MPa	7820 kg/m³	765 J/kg · ℃	50 W/m · K
T4003	280 MPa	450 MPa	7680 kg/m³	510 J/kg · ℃	35 W/m · K

Table 2. Chemical composition of Q450NQR1 (wt%).

Material	C	Si	Mn	P	S	Cu	Cr	Ni	Fe
Q450NQR1	0.12 max	0.75 max	1.5 max	0.025 max	0.008 max	0.20~0.50	0.30~1.25	0.12~0.65	Balance

Table 3. Chemical composition of T4003 (wt%).

Material	C	Si	Mn	P	S	Ni	Cr	N	Fe
T4003	0.030	1.00	1.00	0.040	0.015	0.30~1.00	10.50~12.50	0.030	Balance

Table 4. Welding process parameters.

Material	Power (W)	Welding Speed (mm/s)	Wire Feeding Speed (mm/min)	Spot Diameter (mm)	Number of Welding Passes
T4003	1300	3.50	65	0.2	2
Q450NQR1	950	3.20	60	0.2	2

The fatigue specimens were transversely sectioned from the welded test plates using an electric spark cutting machine, in compliance with GB/T3075-2008 [45]. The detailed dimensions of the fatigue specimens are provided in Figure 4. The experiment was conducted on a PLG-50 fatigue testing machine(Letry Corporation, Xi'an, China) at an ambient temperature of 20 °C. Since the laser-welded joints used in this study were associated with railway locomotive and rolling-stock applications, a stress ratio of R = 0.1 was selected to more accurately represent the in-service loading conditions of these components. Because the applied stress level in the high-cycle fatigue test was relatively low, a loading frequency of 120 Hz was employed to induce a measurable temperature rise on the specimen surface. A minimum of five stress levels were selected for two types of butt joints to perform high-cycle fatigue tests under uniaxial, sinusoidal loading conditions. The fatigue damage entropy was calculated using the same five stress levels, as presented in Table 5.

Table 5. Fatigue test stress levels of two types of welded joints.

Welded Joint	R	Δσ/MPa				
T4003 butt welded joints	0.1	252	243	234	216	208
Q450NQR1 butt welded joints		252	243	234	216	208

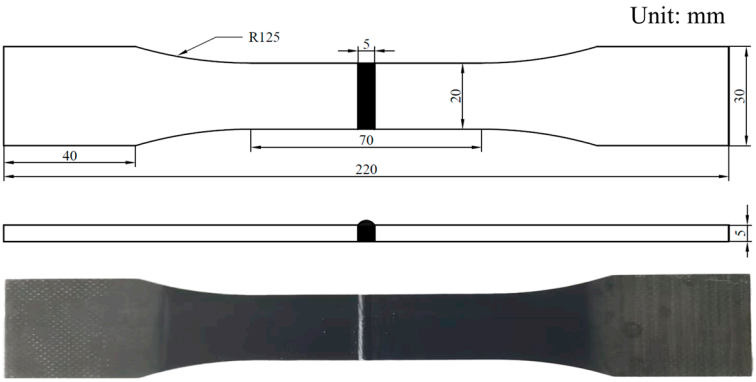


Figure 4. Fatigue Specimen Dimensions and Macroscopic Morphology.

4. Results and Discussion

4.1. S-N Curve Based on Experiment

To verify the theory proposed in Section 2, fatigue tests were conducted. Temperature curves of stainless steel T4003 and weathering steel Q450NQR1 joints were monitored during fatigue tests at varying nominal stress levels to determine the fatigue strength at a specified cycle count of $N = 2 \times 10^6$. As shown in Figure 5, the S-N curve expressions for the stainless steel T4003 welded joints and the weathering steel Q450NQR1 welded joints, derived from the fatigue test, are $\Delta\sigma = 1.262 \times 10^3 N^{-0.1328}$, $\Delta\sigma = 6.561 \times 10^2 N^{-0.0805}$, respectively. Upon calculation, the fatigue strengths are 184 MPa and 204 MPa, respectively, at the specified number of cycles $N = 2 \times 10^6$. Owing to differences in chemical composition and weldability between the two materials, the surface finish of stainless steel T4003 welded joints is inferior. Consequently, the S-N curve data for stainless steel T4003 joints are more scattered than those of weathering steel Q450NQR1 joints.

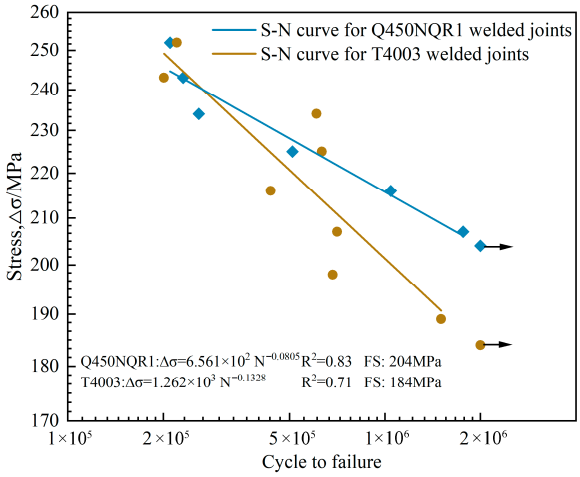


Figure 5. S-N curve of stainless steel T4003 and weathering steel Q450NQR1 welded joints.

4.2. Generation Rate of Entropy

As discussed in Section 2 above, it is generally accepted that the elastic strain energy resulting from elastic behavior does not contribute to the fatigue damage of the material, while the plastic strain energy is the primary cause of fatigue damage and even fracture of the material [39]. Studies on homogeneous materials [38] indicate that the temperature change slope ΔR_θ and the relative temperature change ΔT_s exhibit a highly convergent linear positive correlation with the stress level and reach a critical value below the fatigue strength. Thus, these parameters serve as the primary basis for determining the fatigue strength, quantitatively analyzing energy dissipation due to elastic and plastic behaviors, and subsequently determining the fatigue damage entropy. In fatigue tests of welded structures, due to local joint morphology and welding deformation, a strong relationship between the temperature change slope ΔR_θ and the relative temperature change ΔT_s and the stress level is not observed in small sample fatigue tests. Thus, these parameters cannot accurately or quantitatively analyze the fatigue damage entropy of welded joints in high-cycle fatigue tests.

Given the critical values of the steady-state temperature ΔT_s and the temperature drop slope R_θ^c at the fatigue strength, the formula $\dot{S} = \frac{Q}{f\Delta T_s} = \frac{\rho c_p R_\theta^c}{f\Delta T_s}$ suggests that there is also a critical value for the entropy generation rates $\dot{S}$ at the fatigue strength. Figure 6 shows the relationship between the entropy generation rates and stress $\Delta\sigma$ in each cycle of stainless steel T4003 and weathering steel Q450NQR1 joints. It can be seen that the entropy generation rates above the fatigue strength are in a proportional linear relationship with the stress. Through the $\dot{S}$-$\Delta\sigma$ relationship, the critical entropy generation rates of the two materials at fatigue strength are $1.51\,\mathrm{J/m^3 \cdot K \cdot Cycle}$ and $0.21\,\mathrm{J/m^3 \cdot K \cdot Cycle}$, respectively. It is important to emphasize that the entropy generation rate discussed here pertains to the increase in total entropy during the fatigue test, rather than the rate of fatigue damage entropy.

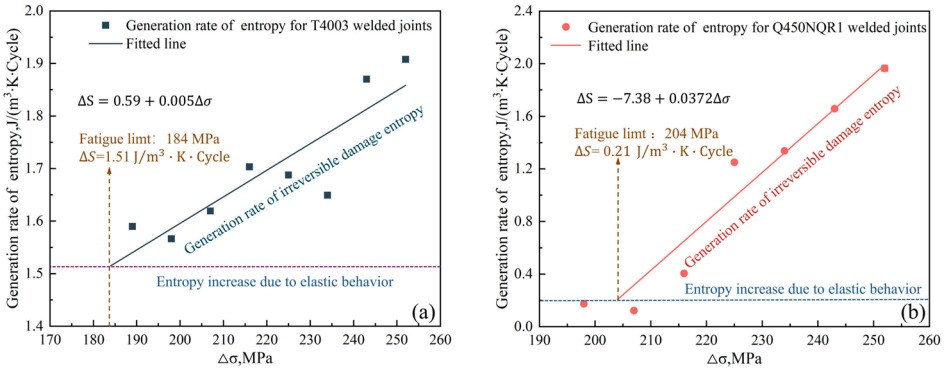


Figure 6. Schematic of the entropy generation rate as a function of stress for welded joints. (**a**) Entropy generation rate vs. stress level for stainless steel T4003 joints. (**b**) Entropy generation rate vs. stress level for weathering steel Q450NQR1 joints.

Stainless steel T4003 has a lower elastic modulus and specific heat capacity. As shown in Equation (10), the stainless steel T4003 joint reaches a higher steady-state temperature at an equivalent stress level. In comparison to the absolute value of the elastic modulus of the welded joints of both materials, the difference in steady-state temperature ΔT_s is negligible. Thus, the entropy generation rate of the stainless steel T4003 joint is higher than that of the weathering steel Q450NQR1 at the same stress level. The expression for entropy increase in each cycle between different stress levels is given by $\Delta S = \frac{\rho c_p \Delta R_\theta^c}{f \Delta T_s}$, where ΔT_s and ΔR_θ^c represent the difference in steady-state temperature at different stress levels during fatigue testing and the temperature change rate at the steady-state temperature during the cooling stage. Due to its higher elastic modulus, density, specific heat capacity, and thermal conductivity compared to stainless steel T4003, when the absolute changes in stress levels of the welded joints of these two materials are the same, the change in $\frac{\Delta R_\theta^c}{\Delta T_s}$ for weathering steel Q450NQR1 is greater than that for stainless steel T4003. Therefore, when the stress level above the fatigue strength changes, the change in the entropy generation rate of weathering steel Q450NQR1 is greater than that of stainless steel T4003. The low-cycle fatigue experiment conducted by Mehdizadeh [15] on carbon steel 1018 also indirectly confirmed that the entropy generation rate is related to the physical properties of the material.

Since the entropy generation rate is determined by the specific physical properties and stress level of the joint, the physical properties of the joint materials themselves remain constant during fatigue testing. Therefore, there exists a highly convergent, linear proportional relationship between entropy generation rate and stress level for both stainless steel T4003 and weathering steel Q450NQR1 joints.

The changes in the entropy generation rate of these two types of welded joints with stress levels indicate that the variation in the entropy generation rate of fatigue damage in welded joints is determined by the physical parameters of the specific joint, including density, elastic modulus, specific heat capacity, and thermal conductivity. Under equal stress level changes in different weld joints, the difference in the change rate of fatigue damage entropy generation results from the variation in the physical parameters of the welding materials. This confirms that fatigue damage entropy is solely determined by material properties.

4.3. Fatigue Damage Entropy of Welded Joints

The trends in total entropy and entropy increase due to elastic behavior with stress for the stainless steel T4003 and weathering steel Q450NQR1 joints are shown in Figure 7. As shown in Section 4.2, the entropy increase due to elastic deformation remains constant

during each stress cycle. Therefore, at stress levels exceeding the fatigue strength, the entropy increase from elastic deformation typically scales proportionally with the number of cycles. Simultaneously, given that fatigue damage entropy remains constant, the total entropy increase during the fatigue failure process correlates directly with the entropy increase caused by elastic behavior.

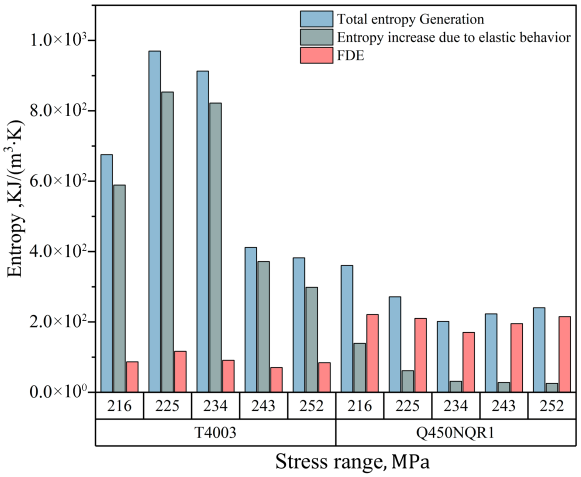


Figure 7. Relationship between entropy increment and stress level of stainless steel T4003 and weathering steel Q450NQR1 welded joints.

The cycle life and entropy production rate of fatigue specimens are influenced by weld surface morphology, welding-induced deformation, and residual stress. Therefore, for weathering steel Q450NQR1 joints and stainless steel T4003 joints, both the total entropy and the entropy increase due to elastic deformation fluctuate within the stress range of 216–252 MPa, but generally exhibit an increasing trend with rising stress levels.

According to the test results in Tables 6 and 7, unlike low-cycle fatigue tests where the entropy increase caused by elastic behavior can be disregarded, this entropy increase constitutes a significant proportion of the total in the high-cycle fatigue failure process of welded joints. Therefore, in analyzing high-cycle fatigue failure problems based on fatigue damage entropy, consideration of the entropy increase caused by elastic behavior is crucial for ensuring the accuracy of prediction models. From Tables 6 and 7, it is observed that the entropy increase caused by elastic behavior accounts for 0.87 and 0.21 of the total entropy for two types of welded joints, respectively. According to Equation (10), the entropy generation rate caused by elastic behavior is inversely proportional to the elastic modulus. Thus, the proportion of entropy increase caused by elastic behavior in the stainless steel T4003 joint to the total entropy is significantly higher than that in the weathering steel Q450NQR1 joint. Despite the increase in entropy caused by elastic behavior with decreasing stress levels, it does not result in a larger proportion of elastic entropy in total entropy generation. This finding further indicates that, under a given welded joint geometry and loading configuration, the fatigue damage entropy is predominantly governed by the material properties [18].

Table 6. Entropy increase statistics of stainless steel T4003 welded joints.

Welded Joint	$\Delta\sigma$/MPa	Total Entropy $kJ/m^3 \cdot K$	Elastic Entropy $kJ/m^3 \cdot K$	FDE $kJ/m^3 \cdot K$	Elastic Entropy/ Total Entropy	FDE/Total Entropy
T4003 butt welded joints	252	382	298	84	0.78	0.22
	243	412	371	70	0.90	0.10
	234	913	822	91	0.90	0.10

	225	970	853	116	0.88	0.12
	216	675	589	87	0.87	0.13
Average value		670	587	90	0.87	0.13
Standard deviation of FDE					13.67	

Table 7. Entropy increase statistics of weathering steel Q450NQR1 welded joints.

Welded Joint	Δσ/MPa	Total Entropy $kJ/m^3 \cdot K$	Elastic Entropy $kJ/m^3 \cdot K$	FDE $kJ/m^3 \cdot K$	Elastic Entropy/ Total Entropy	FDE/Total Entropy
Q450NQR1 butt welded joints	252	240	25	215	0.10	0.90
	243	223	28	195	0.13	0.87
	234	201	31	170	0.15	0.85
	225	371	61	310	0.16	0.84
	216	500	179	321	0.24	0.76
Average value		307	65	242	0.21	0.79
Standard deviation of FDE					56.24	

According to Equation (13), the entropy increase from elastic behavior, which does not contribute to fatigue damage, is subtracted from the total entropy to obtain the fatigue damage entropy for welded joints of two different materials, as shown in Figure 8. The fatigue damage entropy of the joints made from stainless steel T4003 and weathering steel Q450NQR1 are 90 KJ/m³·K and 242 KJ/m³·K, respectively.

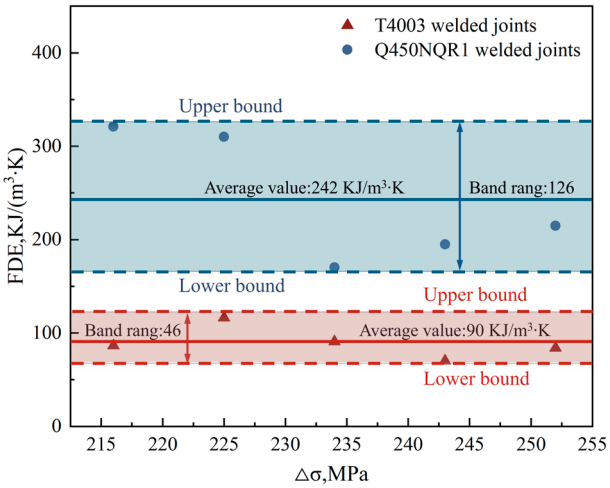


Figure 8. Fatigue damage entropy of two types of welded joints of weathering steel Q450NQR1 and stainless steel T4003.

4.4. S-N Curve Prediction

In Sections 4.1 and 4.2, the entropy generation rate and fatigue damage entropy of weathering steel Q450NQR1 and stainless steel T4003 in the fatigue failure process have been discussed in detail, and the fatigue damage entropy of the welded joints of the two different materials has been obtained. Thus, the fatigue life of the joint at different stress levels can be calculated using Equation (13), and the S-N curve can be fitted accordingly.

Figure 9 shows the S-N curve obtained from the test and based on fatigue damage entropy. For the fatigue strength of weathering steel Q450NQR1 at the specified fatigue life $N = 2 \times 10^6$, the S-N curve obtained from the experiment and the S-N curve calculated based on fatigue damage entropy are 184 MPa and 186 MPa, respectively; the fatigue

strength of stainless steel T4003 at the specified fatigue life of $N = 2 \times 10^6$ are 204 MPa (experimental) and 211 MPa (calculated based on fatigue damage entropy). The relative errors between the fatigue strength obtained from tests on weathering steel Q450NQR1 and stainless steel T4003 joints and those predicted using fatigue damage entropy are 3.4% and 1.1%, respectively.

As pointed out in Section 4.1, owing to the poor weldability of stainless steel T4003 and the suboptimal surface morphology of the weld, the actual local stress state during fatigue testing may deviate from the nominal stress adopted in this study. Consequently, for stainless steel T4003 joints, the S–N curve derived from fatigue damage entropy and that obtained from conventional fatigue testing exhibit considerable scatter.

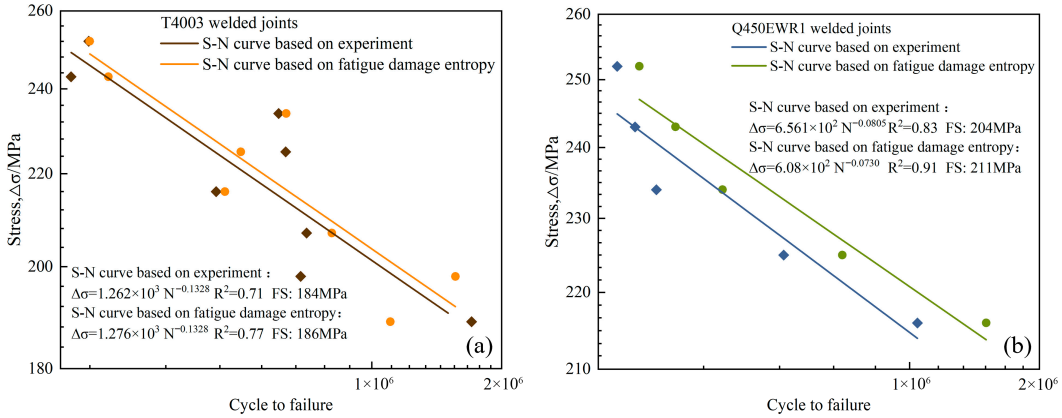


Figure 9. Comparison of S-N curves based on fatigue damage entropy and experimental results: (**a**) Stainless steel T4003 welded joint; (**b**) Weathering steel Q450NQR1 welded joint.

5. Conclusions

In this paper, considering the proportion of entropy increase caused by elastic behavior in the total entropy generation during the fatigue failure process of welded joints, and the factors affecting the entropy generation rate are analyzed. A new fatigue damage entropy calculation model is proposed based on the temperature drop slope at steady-state conditions, and the results of the proposed model are compared with the experimental results.

(1) Owing to differences in physical properties (e.g., specific heat capacity and density) and mechanical properties between the two materials, the fatigue damage entropy production rates of stainless steel T4003 and weathering steel Q450NQR1 joints differ under the same stress level.

(2) In high-cycle fatigue tests of welded joints, the increase in entropy due to elastic behavior, which does not contribute to fatigue damage, varies directly with the number of cycles and inversely with the elastic modulus of the material. For joints made of stainless steel T4003 and weathering steel Q450NQR1, the component of entropy increase constitutes 87% and 21% of the total entropy, respectively. Therefore, in high-cycle fatigue tests, the calculation of fatigue damage entropy necessitates subtracting the entropy increase due to elastic behavior from the total entropy to obtain an accurate measure of fatigue damage entropy.

(3) For a specific welded joint, the fatigue damage entropy is a thermodynamic parameter related solely to the material properties. In this study, the fatigue damage entropies of the joints of stainless steel T4003 and weathering steel Q450NQR1 are determined to be 90 kJ/m³·K and 242 kJ/m³·K, respectively.

(4) Under the specified fatigue life $N = 2 \times 10^6$, the fatigue strength obtained from the fatigue tests of the welded joints of stainless steel T4003 and weathering steel

Q450NQR1, as well as those obtained based on fatigue damage entropy, exhibit errors of 1.1% and 3.4%, respectively. This further demonstrates the effectiveness and accuracy of the fatigue damage entropy model proposed in this study.

Author Contributions: Conceptualization, Y.L. and Y.S., Methodology, Y.L. and X.Y., Validation, Y.L. and Y.S., Formal analysis, Y.L. and Y.S., Investigation, Y.L. and Y.S., Resources, X.Y., Data curation, Y.L., Writing—original draft preparation, Y.L., Writing—review and editing, X.Y., Project administration, X.Y., Funding acquisition, X.Y. All authors have read and agreed to the published version of the manuscript.

Funding: This research received no external funding.

Data Availability Statement: The original contributions presented in the study are included in the article. Further inquiries can be directed to the corresponding author.

Acknowledgments: The authors would like to thank Dalian Jiaotong University for providing instrumental support for the fatigue temperature measurements.

Conflicts of Interest: The authors declare no conflicts of interest.

Nomenclature

R_θ	the temperature rise slope, ℃/s
Q_t	the total energy dissipation, kJ
Q_f	internal friction, kJ
Q_i	the irreversible energy dissipation, kJ
ΔT_s	the steady-state temperature (the temperature rise in the sample surface relative to its initial temperature), K
$\dot{E}_{in}$	the heat transferred from the environment to the specimen, kJ
$\dot{E}_{out}$	the heat dissipated from the specimen to the environment, kJ
$\dot{E}_{gen}$	the energy input to the specimen due to externally applied cyclic stress, kJ
$\dot{S}$	the entropy increase in each cycle, $\mathrm{kJ/m^3 \cdot K \cdot Cycle}$
U	the internal energy, kJ
σ	stress, MPa
FS	fatigue strength, MPa
ρ	material density, $\mathrm{kg/m^3}$
c_p	specific heat capacity, $\mathrm{J/kg \cdot ℃}$
Q_p	the energy dissipated due to plastic deformation, kJ
R_θ^c	the temperature drop slope, ℃/s
R_θ^e	the temperature drop slope that does not contribute to fatigue damage, ℃/s
N	the number of loading cycles
f	the loading frequency, Hz
FDE	fatigue damage entropy, $\mathrm{kJ/m^3 \cdot K}$

References

1. Di, H.S.; Sun, Q.; Wang, X.N.; Li, J.P. Microstructure and properties in dissimilar/similar weld joints between DP780 and DP980 steels processed by fiber laser welding. *J. Mater. Sci. Technol.* **2017**, *33*, 1561–1571. https://doi.org/10.1016/j.jmst.2017.09.001.
2. Xu, Z.W.; Wu, S.C.; Wang, X.S. Fatigue evaluation for high-speed railway axles with surface scratch. *Int. J. Fatigue* **2019**, *123*, 79–86. https://doi.org/10.1016/j.ijfatigue.2019.02.016.
3. Zhang, W.Y.; Song, M.; Jiang, W.C.; Sun, G.G.; Shan, G.B.; Chen, M.D.; Bai, Y.Z. Fatigue failure mechanism of 2205 duplex stainless steel using the neutron diffraction and EBSD technologies. *Int. J. Fatigue* **2022**, *159*, 106828. https://doi.org/10.1016/j.ijfatigue.2022.106828.
4. Cao, Y.F.; Moumni, Z.; Zhu, J.H.; Zhang, Y.H.; You, Y.J.; Zhang, W.H. Comparative investigation of the fatigue limit of additive-manufactured and rolled 316 steel based on self-heating approach. *Eng. Fract. Mech.* **2020**, *223*, 106746. https://doi.org/10.1016/j.engfracmech.2019.106746.

5. De Finis, R.; Palumbo, D.; Ancona, F.; Galietti, U. Fatigue limit evaluation of various martensitic stainless steels with new robust thermographic data analysis. *Int. J. Fatigue* **2015**, *74*, 88–96. https://doi.org/10.1016/j.ijfatigue.2014.12.010.
6. Palumbo, D.; De Finis, R.; Ancona, F.; Galietti, U. Damage monitoring in fracture mechanics by evaluation of the heat dissipated in the cyclic plastic zone ahead of the crack tip with thermal measurements. *Eng. Fract. Mech.* **2017**, *181*, 65–76. https://doi.org/10.1016/j.engfracmech.2017.06.017.
7. Luong, M.P. Fatigue Limit Evaluation of Metals Using an Infrared Thermographic Technique. *Mech. Mater.* **1998**, *28*, 155–163. https://doi.org/10.1016/S0167-6636(97)00047-1.
8. Luong, M.P. Infrared thermographic scanning of fatigue in metals. *Nucl. Eng. Des.* **1995**, *158*, 363–376. https://doi.org/10.1016/0029-5493(95)01043-h.
9. Geraci, A.L.; La Rosa, G.; Risitano, A.; Grech, M. Determination of the fatigue limit of an austempered ductile iron using thermal infrared imagry. In Proceedings of the Digital Photogrammetry and Remote Sensing '95, St. Petersburg, Russia, 25–30 June 1995; Volume 2646, pp. 306–317.
10. La Rosa, G.; Risitano, A. Thermographic methodology for rapid determination of the fatigue limit of materials and mechanical components. *Int. J. Fatigue* **2000**, *22*, 65–73. https://doi.org/10.1016/s0142-1123(99)00088-2.
11. Amiri, M.; Khonsari, M.M. Rapid determination of fatigue failure based on temperature evolution: Fully reversed bending load. *Int. J. Fatigue* **2010**, *32*, 382–389. https://doi.org/10.1016/j.ijfatigue.2009.07.015.
12. Mehdizadeh, M.; Khonsari, M.M. On the application of fracture fatigue entropy to multiaxial loading. *Int. J. Fatigue* **2021**, *150*, 106321. https://doi.org/10.1016/j.ijfatigue.2021.106321.
13. Jirandehi, A.P.; Khonsari, M.M. Microstructure-sensitive estimation of fatigue life using cyclic thermodynamic entropy as an index for metals. *Theor. Appl. Fract. Mech.* **2021**, *112*, 102854. https://doi.org/10.1016/j.tafmec.2020.102854.
14. Liakat, M.; Khonsari, M.M. Rapid estimation of fatigue entropy and toughness in metals. *Mater. Des.* **2014**, *62*, 149–157.
15. Mehdizadeh, M.; Khonsari, M.M. On the role of internal friction in low-and highcycle fatigue. *Int. J. Fatigue* **2018**, *114*, 159–166. https://doi.org/10.1016/j.ijfatigue.2018.05.007.
16. Amooie, M.A.; Khonsari, M.M. On the effect of environmental temperature on fracture fatigue entropy. *Int. J. Fatigue* **2023**, *168*, 107411. https://doi.org/10.1016/j.ijfatigue.2022.107411.
17. Mahmoudi, A.; Khonsari, M.M. Investigation of metal fatigue using a coupled entropy-kinetic model. *Int. J. Fatigue* **2022**, *161*, 106907. https://doi.org/10.1016/j.ijfatigue.2022.106907.
18. Naderi, M.; Amiri, M.; Khonsari, M.M. On the thermodynamic entropy of fatigue fracture. *Proc. R. Soc. A Math. Phys. Eng. Sci.* **2010**, *466*, 423–438. https://doi.org/10.1098/rspa.2009.0348.
19. Skibicki, D.; Pejkowski, Ł. Low-cycle multiaxial fatigue behaviour and fatigue life prediction for CuZn37 brass using the stress-strain models. *Int. J. Fatigue* **2017**, *102*, 18–36. https://doi.org/10.1016/j.ijfatigue.2017.04.011.
20. Ummenhofer, T.; Medgenberg, J. On the use of infrared thermography for the analysis of fatigue damage processes in welded joints. *Int. J. Fatigue* **2009**, *31*, 130–137. https://doi.org/10.1016/j.ijfatigue.2008.04.005.
21. Wei, W.; Du, L.; Zhang, Y.T.; Sun, Y.; Yang, X.H. Fatigue reliability evaluation of Q460 welded joints using fracture fatigue entropy method. *Eng. Fract. Mech.* **2021**, *247*, 107641. https://doi.org/10.1016/j.engfracmech.2021.107641.
22. Wei, W.; He, L.; Chen, M.H.; Chen, X.T.; Liang, R.Y.; Zou, L.; Yang, X.H. A twoscale thermodynamic entropy model for rapid high-cycle fatigue property evaluation of welded joints. *Eng. Fract. Mech.* **2023**, *292*, 109614. https://doi.org/10.1016/j.engfracmech.2023.109614.
23. Wei, W.; Sun, Y.; Chen, M.H.; Zhao, X.M.; Tang, Y.; Zou, L.; Yang, X.H. Rapid fatigue life prediction of butt joint using energy dissipation. *Int. J. Mech. Sci.* **2023**, *245*, 108109. https://doi.org/10.1016/j.ijmecsci.2023.108109.
24. Crupi, V.; Guglielmino, E.; Maestro, M.; Marinò, A. Fatigue analysis of butt welded AH36 steel joints: Thermographic method and design S–N curve. *Mar. Struct.* **2009**, *22*, 373–386. https://doi.org/10.1016/j.marstruc.2009.03.001.
25. Yan, Z.F.; Zhang, H.X.; Wang, W.X.; He, X.L.; Liu, X.Q.; Wu, G.H. Temperature evolution mechanism of AZ31B magnesium alloy during high-cycle fatigue process. *Theor. Appl. Fract. Mech.* **2014**, *70*, 30–38. https://doi.org/10.1016/j.tafmec.2014.03.003.
26. Zaeimi, M.; De Finis, R.; Palumbo, D.; Galietti, U. Fatigue limit estimation of metals based on the thermographic methods: A comprehensive review. *Fatigue Fract. Eng. Mater. Struct.* **2024**, *47*, 611–646. https://doi.org/10.1111/ffe.14206.
27. Pirinu, A.; Panella, F.W. A new approach for rapid fatigue limit assessment for C45 steel based on contrast damage parameters. *Mech. Res. Commun.* **2023**, *127*, 104039. https://doi.org/10.1016/j.mechrescom.2022.104039.
28. Yu, H.; Hu, Y.N.; Kang, G.Z.; Peng, X.; Chen, B.Q.; Wu, S.C. High-cycle fatigue life prediction of L-PBF AlSi10Mg alloys: A domain knowledge-guided symbolic regression approach. *Philos. Trans. R. Soc. A* **2024**, *382*, 20220383. https://doi.org/10.1098/rsta.2022.0383.

29. Zhang, Z.J.; An, X.H.; Zhang, P.; Yang, M.X.; Yang, G.; Wu, S.D.; Zhang, Z.F. Effects of dislocation slip mode on high-cycle fatigue behaviors of ultrafine-grained Cu–Zn alloy processed by equal-channel angular pressing. *Scr. Mater.* **2013**, *68*, 389–392. https://doi.org/10.1016/j.scriptamat.2012.10.036.
30. Mughrabi, H.; Höppel, H.W. Cyclic deformation and fatigue properties of very fine-grained metals and alloys. *Int. J. Fatigue* **2010**, *32*, 1413–1427. https://doi.org/10.1016/j.ijfatigue.2009.10.007.
31. An, X.H.; Wu, S.D.; Wang, Z.G.; Zhang, Z.F. Enhanced cyclic deformation responses of ultrafine-grained Cu and nanocrystalline Cu–Al alloys. *Acta Mater.* **2014**, *74*, 200–214. https://doi.org/10.1016/j.actamat.2014.04.053.
32. Wang, B.B.; An, X.H.; Xue, P.; Liu, F.C.; Ni, D.R.; Xiao, B.L.; Liu, Y.D.; Ma, Z.Y. Grain size effects on high cycle fatigue behaviors of pure aluminum. *Int. J. Fatigue* **2023**, *170*, 107556. https://doi.org/10.1016/j.ijfatigue.2023.107556.
33. Meneghetti, G. Analysis of the fatigue strength of a stainless steel based on the energy dissipation. *Int. J. Fatigue* **2007**, *29*, 81–94. https://doi.org/10.1016/j.ijfatigue.2006.02.043.
34. Lee, H.T.; Chen, J.C.; Wang, J.M. Thermomechanical behaviour of metals in cyclic loading. *J. Mater. Sci.* **1993**, *28*, 5500–5507. https://doi.org/10.1007/bf00367821.
35. Yang, W.P.; Fan, J.L.; Guo, Q.; Guo, X.L. Experimental procedure for energy dissipation estimation during high-cycle fatigue loading of metallic material. *Exp. Mech.* **2020**, *60*, 695–712. https://doi.org/10.1007/s11340-020-00589-2.
36. Guo, Q.; Guo, X.L.; Fan, J.L.; Rizwanulhaque, S.; Wu, C.W. An energy method for rapid evaluation of high-cycle fatigue parameters based on intrinsic dissipation. *Int. J. Fatigue* **2015**, *80*, 136–144. https://doi.org/10.1016/j.ijfatigue.2015.04.016.
37. Guo, Q.; Guo, X.L. Research on high-cycle fatigue behavior of FV520B stainless steel based on intrinsic dissipation. *Mater. Des.* **2016**, *90*, 248–255. https://doi.org/10.1016/j.matdes.2015.10.103.
38. Maquin, F.; Pierron, F. Heat dissipation measurements in low stress cyclic loading of metallic materials: From internal friction to micro-plasticity. *Mech. Mater.* **2009**, *41*, 928–942. https://doi.org/10.1016/j.mechmat.2009.03.003.
39. Meneghetti, G.; Quaresimin, M. Fatigue strength assessment of a short fiber composite based on the specific heat dissipation. *Compos. Part B Eng.* **2011**, *42*, 217–225. https://doi.org/10.1016/j.compositesb.2010.12.002.
40. Wang, X.G.; Crupi, V.; Guo, X.L.; Zhao, Y.G. Quantitative Thermographic Methodology for fatigue assessment and stress measurement. *Int. J. Fatigue* **2010**, *32*, 1970–1976. https://doi.org/10.1016/j.ijfatigue.2010.07.004.
41. Salimi, H.; Pourgol-Mohammad, M.; Yazdani, M. Metal fatigue assessment based on temperature evolution and thermodynamic entropy generation. *Int. J. Fatigue* **2019**, *127*, 403–416. https://doi.org/10.1016/j.ijfatigue.2019.06.022.
42. Liakat, M.; Khonsari, M.M. On the anelasticity and fatigue fracture entropy in highcycle metal fatigue. *Mater. Des.* **2015**, *82*, 18–27. https://doi.org/10.1016/j.matdes.2015.04.034.
43. Wang, S.F.; Peng, Y.; Li, Z.J. Work-Hardening and Deformation Mechanism of Cold Rolled Low Carbon Steel. *Res. J. Apll. Sci. Eng. Technol.* **2013**, *5*, 823–828. http://doi.org/10.19026/rjaset.5.5028.
44. Deva, A.; Jha, B.K.; Mishra, N.S. Influence of boron on strain hardening behaviour and ductility of low carbon hot rolled steel. *Mater. Sci. Eng. A* **2011**, *528*, 7375–7380. https://doi.org/10.1016/j.msea.2011.06.030.
45. *GB/T3075-2008*; Metallic Materials—Fatigue Testing—Axial Force Control Methods. China Standards Press: Beijing, China, 2008.

Disclaimer/Publisher's Note: The statements, opinions and data contained in all publications are solely those of the individual author(s) and contributor(s) and not of MDPI and/or the editor(s). MDPI and/or the editor(s) disclaim responsibility for any injury to people or property resulting from any ideas, methods, instructions or products referred to in the content.